RESEARCH ARTICLE

NANO · MICRO small
www.small-journal.com

Velocity-Switched Droplet Rebound Direction on Anisotropic Superhydrophobic Surfaces

*Peiliu Li, Fei Zhan, and Lei Wang**

Droplet well-controlled directional motion being an essential function has attracted much interest in academic and industrial applications, such as self-cleaning, micro-/nano-electro-mechanical systems, drug delivery, and heat-transferring. Conventional understanding has it that a droplet impacted on an anisotropic surface tends to bounce along the microstructural direction, which is mainly dictated by surface properties rather than initial conditions. In contrast to previous findings, it demonstrates that the direction of a droplet's rebound on an anisotropic surface can be switched by designing the initial impacting velocity. With an increase in impacting height from 2 to 10 cm, the droplet successively shows a backward, vertical, and forward motion on anisotropic surfaces. Theoretical demonstrations establish that the transition of droplet bouncing on the anisotropic surface is related to its dynamic wettability during impacting process. Characterized by the liquid-solid interaction, it is demonstrated that the contact state at small and large impacting heights induces an opposite resultant force in microstructures. Furthermore, energy balance analysis reveals that the energy conversion efficiency of backward motion is almost three times as that of traditional bouncing. This work, including experiments, theoretical models, and energy balance analysis provides insight view in droplet motions on the anisotropic surfaces and opens a new way for the droplet transport.

1. Introduction

The directed and long-range transport of droplets on solid surfaces being a universal function with a variety of outstanding properties has been widely investigated and used in fundamental studies and applications, such as water harvesting,[1–5] self-cleaning,[6–8] and heat-transferring.[9,10] Owing to the fact that the directional transport of droplets is very important in applications, several strategies have been pursued to manipulate the conditions to achieve preferential transport, including coercive and self-propelled methods. Examples of coercive methods that induce a directional motion of liquid droplets are generally achieved by applying external fields, including electric,[11,12] magnetic,[13,14] and thermal[15,16] fields. In addition, there are approaches that achieve directional bouncing by controlling the incident angle and velocity of the droplets.[17–21] Self-propelled methods are achieved by surface heterogeneity,[22–24] topographic,[25–28] chemical modulation,[29,30] and electrical modification of surface-wetting gradients,[31] which disrupt the asymmetric contact line and overcome resistance forces to drive droplets along a specific direction. While both methods can achieve directed droplet transport, self-propelled methods are preferred in applications due to their simplicity and low energy consumption.

In contrast to chemical modulation and electrical modification of surface-wetting gradients, the directional transport of droplets achieved by topography can serve as a simple physical self-propelled method that is realized by the asymmetric liquid–solid interaction. For instance, substrates with gradient micro-structures induce liquid droplets impacting the surface to move toward regions with larger scales,[32] micro-patterned surfaces inhibit droplet breakage,

P. Li, L. Wang
Beijing Key Lab of Cryo-biomedical Engineering and Key Lab of Cryogenics
Technical Institute of Physics and Chemistry
Chinese Academy of Sciences
Beijing 100190, China

L. Wang
Beijing Key Laboratory of Lignocellulosic Chemistry
Beijing Forestry University
Beijing 100083, China
E-mail: leiwang@mail.ipc.ac.cn

P. Li
Biomechanics and Biomaterials Laboratory
Department of Mechanics
School of Aerospace Engineering
Beijing Institute of Technology
Beijing 100081, China

P. Li
State Key Laboratory of Nonlinear Mechanics
Institute of Mechanics
Chinese Academy of Sciences
Beijing 100190, China

F. Zhan
School of Electrical and Electronic Engineering
Shijiazhuang Tiedao University
Shijiazhuang 050043, China

The ORCID identification number(s) for the author(s) of this article can be found under https://doi.org/10.1002/smll.202305568

DOI: 10.1002/smll.202305568

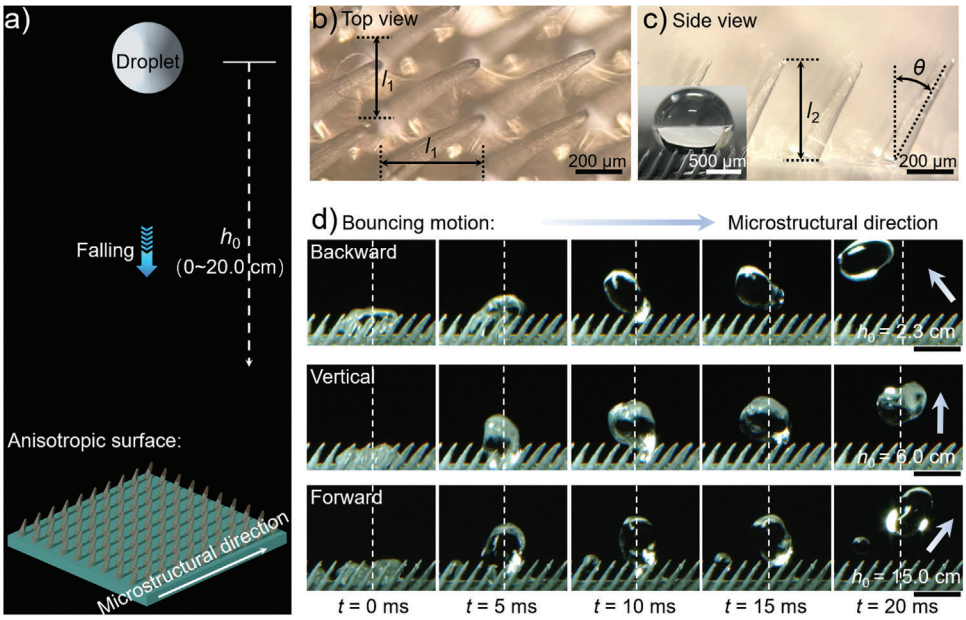

Figure 1. Experimental setup and the characteristics of microstructure for droplet bouncing transition. a) Experimental apparatus setup. The liquid droplet with a volume of V_0 is freely dripped at the impacting height of h_0. Microstructural direction is the horizontal project orientation of the microstructures. b,c) SEM images of microstructural topography on the anisotropic superhydrophobic surface. The space l_1, height l_2, and tilt angle θ of the microstructural array are 300 μm, 300 μm, and 30°, respectively. The contact angle of a liquid droplet with a volume of 10 μL on the anisotropic surface is ≈150°. d) Transitions of droplet bouncing motion on the anisotropic superhydrophobic surface. At the impacting height of 2.3, 6.0, and 15.0 cm, liquid droplet bounces against, perpendicular to, and along the microstructural direction, respectively. White dashed lines are the centerline of the droplet as it impacts. The scale bars in (d) are 2 mm.

enabling directional bouncing,[33] and anisotropic microstructures induce the asymmetric solid–liquid–gas three-phase contact lines in the impacting process,[34] facilitating directed transport. Wherein the surfaces fabricated with anisotropic microstructures are widely employed for directed droplet transport, both in natural biology and artificial products. Recent research has shown that the contact state in the microstructural array would be affected by the initial condition, which may change the liquid–solid interaction on an anisotropic surface.[10,35–40] Due to the complexity of microstructural parameters, clarifying the solid–liquid–gas three-phase contact lines in the impacting process is challenging. Understanding the evolution of liquid–solid interaction on anisotropic surfaces is crucial for explaining directed droplet transport. In addition, the droplet impacted the anisotropic surface involves the conversion of gravitational potential energy into horizontal kinetic energy of liquid droplets. Without this conversion, the droplet would break up due to its large gravitational potential energy, resulting in short-range transport. Therefore, achieving a long-distance, self-propelled, and controllable on the anisotropic surface remains a big challenge.

In this study, we investigated the bouncing behavior of liquid droplets on an anisotropic surface featuring an inclined microcone array wherein low-impacting-velocity liquid droplets follow a pathway opposite to the microstructure-tilting direction, while high-impacting-velocity liquid droplets tend to bounce along the microstructure-tilting direction. In contrast to conventional understanding, the liquid droplet presents different contact states at a low and high impacting velocity, resulting in distinct loading conditions that determine the bouncing motion. Moreover, by comparing the energy conversion efficiency, it is demonstrated that the new way of droplet transport on an anisotropic surface would be preferable for high energy conversion efficiency and transport sustainability.

2. Results

2.1. Experimental Setup and the Characterization of Droplet Bouncing Motion

Figure 1a shows an experimental setup of the droplet bouncing motion on the anisotropic superhydrophobic surface that mainly includes three core elements: an anisotropic superhydrophobic surface, a micropump, and a height adjuster. Initially, the anisotropic superhydrophobic surface was fabricated using soft lithography and crystal growth methods (see Experimental Section). Optical and SEM images of microstructural topography and nano-modified characterization on the anisotropic superhydrophobic surface are presented in Figure 1b,c and Figure S1 (Supporting Information), respectively. It is shown that an inclined cone array on the tested surface has a height l_2 of 300 μm, a space l_1 of 300 μm, and an inclined angle θ of 30°, and ZnO nano-rods were used to improve the surface roughness and low hysteresis. The contact angle of the anisotropic superhydrophobic surface is ≈150° and the sliding angle is shown in Figure S2 (Supporting Information). Second, a liquid droplet with a volume of V_0 was freely released at the height of h_0 directly above the anisotropic superhydrophobic surface. This releasing height h_0 is defined as the droplet impacting height that is altered precisely by the height adjuster (see Experimental Section). After the

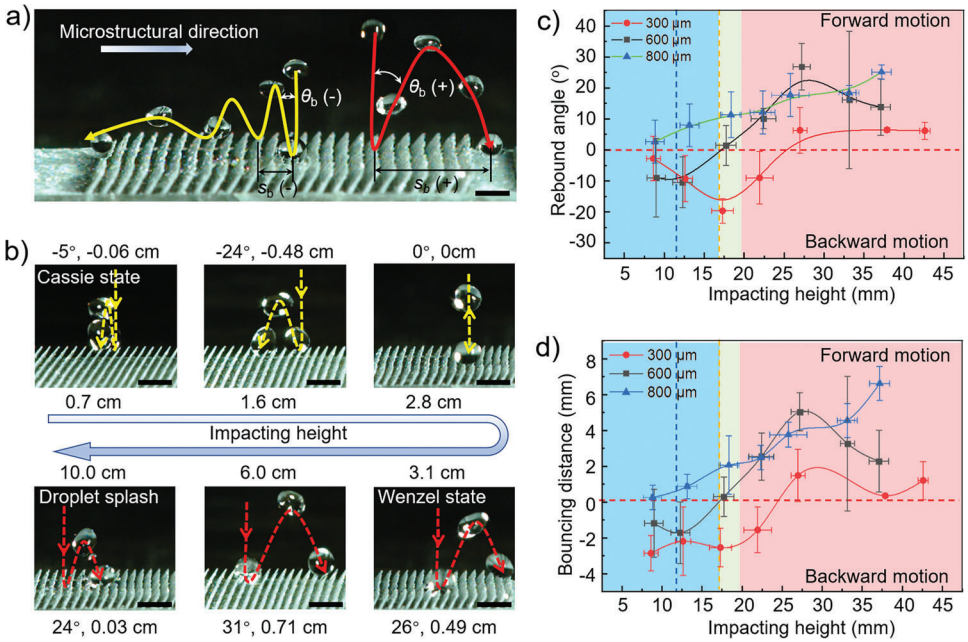

Figure 2. Transitions of droplet bouncing motion on the anisotropic surface. a) Characterization of droplet bouncing motion on the anisotropic surface. s_b and θ_b are the bouncing distance and the rebound angle, respectively. b) Liquid droplet rebound track on the anisotropic surface with various impacting heights. Yellow and red dotted lines label the rebound track of backward/vertical and forward motion. c,d) Statistic results of the droplet bouncing distance and the rebound angle on the anisotropic surface. The blue, green, and red areas are used to mark the impacting height of backward, vertical, and forward motion on the anisotropic surface with various spaces. All experiments were repeated six times, and error bars in (c,d) are the standard deviation of raw data. Here, scale bars in (a,b) are 1 mm.

liquid droplet is freely released, a high-speed camera is used to capture its behavior at 1000 frames per second. Contrary to the conventional understanding that a liquid droplet impacted on an anisotropic surface tends to bounce along the microstructural direction, it is observed that the droplet shows three distinct types of bouncing motions at different impacting heights (Figure 1d). At an impacting height of 2.3, 6.0, and 15.0 cm, the droplet bounces along the opposite (backward motion), the vertical (vertical motion), and the same (forward motion) direction as microstructures (Movie S1, Supporting Information). Experimental observations show that the transition of droplet bouncing direction on the anisotropic surface can be controlled by the impacting height.

2.2. Transitions of Droplet Bouncing Motion at Various Impacting Heights

As mentioned above, the liquid droplet bouncing motion shows three types of bouncing motion on the anisotropic surface: Backward, Vertical, and Forward motion. To quantitatively describe the transitions of bouncing motions, observations of the bouncing distance (s_b) and the bouncing angle (θ_b) were conducted with a broad range of impacting heights. Wherein the bouncing distance (s_b) describes the first horizontal bouncing displacement of the droplet, and the bouncing angle (θ_b) represents the included angle between the rebound track and the vertical direction (**Figure 2**a). During the impacting process, both s_b and θ_b are positive, zero, and negative, indicating the forward, vertical, and backward motion, respectively. Figure 2b shows the rebound track of the liquid droplet with the impacting height from 2.0 to 15.0 cm. Observations show that s_b and θ_b initially exhibit negative values at small impacting heights (h_0 = 0.7, 1.6 cm), but subsequently decrease at first and then increase as the impacting height changes from 0.7 to 2.8 cm. When the impacting height is larger than 2.8 cm, both s_b and θ_b are positive, and resulting in a transition of the droplet bouncing motion from the opposite to the same direction of the microstructures. On the contrary, the liquid droplet bouncing distance and angle increase first and subsequently decrease with increasing impacting height. The statistical results of the bouncing distance and angle at various impacting heights are presented in Figure 2c,d. On the three types of anisotropic surfaces (space = 300, 600, 800 μm), the droplet bouncing motion shows a similar relationship with the impacting heights. At the small impacting height (blue area), the liquid droplet tends to bounce in the opposite direction of the microstructures when impacting the anisotropic surface. As the impacting height reaches a critical value (green area), the liquid droplet shows a non-directional bouncing motion, similar to impacting a smooth surface. When the impacting height is larger than the critical value (red area), the liquid droplet motion on the anisotropic surface becomes the well-known result in previous studies[7,9,10] that a droplet impacted on an anisotropic surface tends to bounce along the microstructural direction. In conclusion, the bouncing motion of a liquid droplet on an anisotropic surface is influenced not only by the microstructural topography but also by the initial conditions.

2.3. Working Mechanism and Theoretical Model of Droplet Bouncing Transition

The interaction between the liquid and the solid surface is the primary factor influencing the motion of liquid droplets on the anisotropic surface. To explain the mechanism responsible for the bouncing transition, we first examined the dynamic wetting state of liquid droplet on the anisotropic surface at various impacting heights. Observations presented in **Figure 3**a,b reveal significant variations in the dynamic wetting state at different impacting heights. The droplet with a small impacting height (h_0 = 3.0 cm) only contacts with the top of the microstructure, which is similar to the Cassie state. And the droplet with a large impacting height would wet the whole microstructure and this contact state is similar to the Wenzel state (h_0 = 10.0 cm). These two dynamic contact states have a diverse liquid–solid interaction, to influence the droplet bouncing motion in impacting the process.

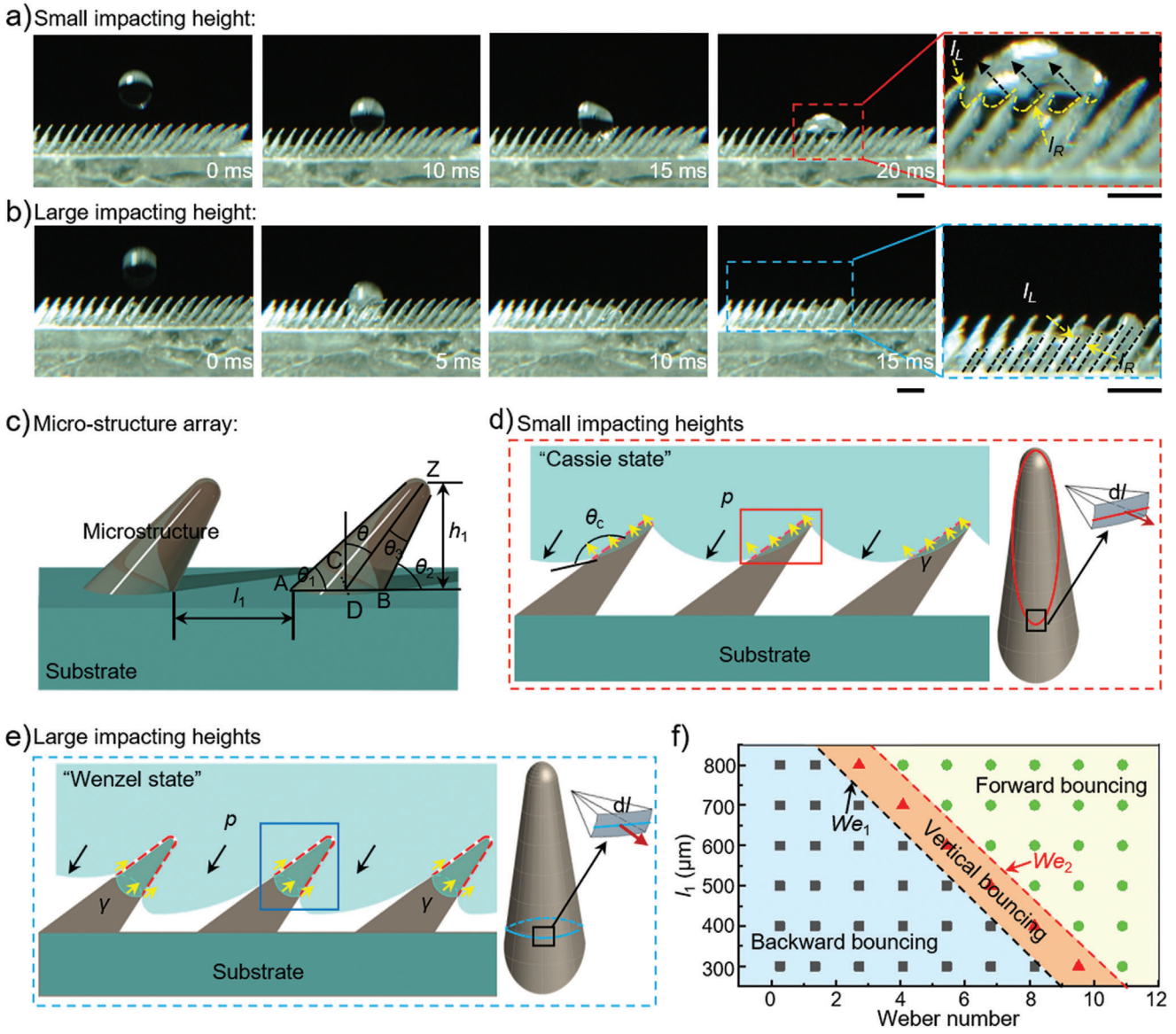

Figure 3. Working mechanism of droplet bouncing motion on the anisotropic surface. a,b) Two distinct wetting sate of droplet on the anisotropic surface. The droplet with an impacting height of 3.5 cm does not wet the microstructural gap, whereas droplet with a impacting height of 10.0 cm wets the microstructural gap. The droplet state in (a,b) is in spreading process at 20 and 15 ms, respectively. The scale bar in (a,b) is 1 cm. c) Characteristics of microstructural array. θ_1, θ_2, and θ_3 are the angles between the bottom surface and the generatrix of the micro-cone for the left and right sides, and the half-apex angle of the axial section of the micro-cone, respectively. d,e) Force analysis of droplet bouncing motion at small and large impacting height. p is dynamic pressure of droplet. γ is the surface tension. The red arrow is used to mark the normal line in the microstructural surface. f) Phase map for the Transition of droplet bouncing motion on the anisotropic surface. When $We > We_2$, the droplet bounces forward (orange region marked with a circle). When $We < We_1$, the droplet bounces backward (blue region marked with a triangle). When $We_1 < We < We_2$, the droplet bounces vertically (blue region marked with a square).

To describe the liquid–solid interaction at the small and large impacting heights, we then resorted to a force analysis to probe how a liquid selects its rebound direction (Figure 3c–e). Liquid droplet with a density of ρ, surface tension of γ, and radius of r_0 is freely released at a height of h_0 (Corresponding to Figure 1a). Due to the working characteristic length of droplet (10^{-3} m) and the release height (10^{-2} m) being much small, the air resistance is neglectable in the falling process. When the droplet impacts the anisotropic superhydrophobic surface, the velocity of droplet $v = \sqrt{2gh_0}$. Substituting the velocity of droplet in the dynamic pressure for convenience, we have

$$\Delta P_d = \frac{\rho v^2}{2} = \rho g h_0 \tag{1}$$

in which g is the gravitational acceleration. Therefore, the dynamic pressure of the droplet is linear with the impacting height. Due to the microstructural array with a micro-gap and a large contact angle, there is a large Laplace pressure needed to be overcome when the liquid droplet wets the microstructure. According to the Young–Laplace equation, the Laplace pressure for wetting microstructures can be described as[35] $\Delta P = \gamma_{lv}(1/r_1 + 1/r_2) \approx 8\gamma_{lv}\delta/l_1^2$, where γ_{lv} is the liquid–vapor interfacial tension, δ is the height of a meniscus between the micro-stripes, r_1 and r_2 are the two principal curvature radii, respectively. Thus, the Laplace pressure on the microstructure is decreased with increasing the microstructural space. Balancing the Laplace pressure with the dynamic pressure, the critical impacting velocity and height can be given as

$$v_c = \sqrt{\frac{16\gamma_{lv}\delta}{\rho l_1^2}},\ h_c = \frac{8\gamma_{lv}\delta}{\rho g l_1^2} \tag{2}$$

Substituting the height of a meniscus and the microstructural space in Equation (2), it could be obtained that the critical impacting heights (h_c) are ≈17.5, 7.1, and 6.4 mm when l_1 is 300, 600, and 800 μm, respectively (Figure S3, Supporting Information). When $h_0 < h_c$, there is a too small dynamic pressure of liquid droplet to overcome the Laplace pressure for wetting the microstructural gap. On the contrary, the liquid droplet would wet microstructural gap when $h_0 > h_c$ (Movie S2, Supporting Information). Corresponding to Figure 2c,d, the critical impacting height is 16.0, 9.0, and 5.6 mm on the anisotropic surface with space of 300, 600, and 800 μm, which increases with the rise of microstructural space that consistent with the theoretical analysis.

When $h_0 < h_c$, the liquid–solid interaction and the contact line are presented in Figure 3d. The resultant force of the surface tension loading on the droplet can be expressed as

$$F_1 = \int_0^{l_t} \gamma \cos\theta_c \sin\theta_3 dl \tag{3}$$

where l_t is the length of the contact line, θ_c is the contact angle and θ_3 is the angle between the normal line of contact point and the ZAB plane (Figure 3d). At this contact state, its 2D physical model is presented in Figure 3d and the resultant force is along the vertical direction of AZ due to the axisymmetric contact line.

When $h_0 > h_c$, the contact line is like a circle shape, the resultant force of surface tension is described by

$$F_2 = \int_0^{l_t} \gamma \cos\theta_c \cos\theta_4 dl \tag{4}$$

in which θ_4 is the half-apex angle of the micro-cone's axial section. Because the surface tension is balanced in the radial direction, F_2 is along the microstructural axial direction. In the impacting process, the liquid–solid wetting state consists of two contact states, and the surface tension loading the droplet induced by microstructures is made by F_1 and F_2. Therefore, the momentum induced by surface tension on the microstructure can be expressed as

$$I = I_1 + I_2 = n_1 \int_0^{t_0}\int_0^{l_t} \gamma \cos\theta_c \cos\theta_4 dl dt - n_2 \int_0^{t_0}\int_0^{l_t} \gamma \cos\theta_c \cos\theta_3 dl dt \tag{5}$$

where $I_1 = n_1 \int_0^{t_0}\int_0^{l_t} \gamma \cos\theta_c \cos\theta_4 dl dt$, $I_2 = -n_2 \int_0^{t_0}\int_0^{l_t} \gamma \cos\theta_c \sin\theta_3 dl dt$, t_0 is the rebound time, n_1 and n_2 are the number of micro-structures contacted with the droplet in "Cassie and Wenzel states", respectively. Interfering from Equation (2), we obtain there is only the first contribution, I_1, to dominate the droplet rebound motion when $h_0 < h_c$. At such liquid–solid interaction, the droplet would prefect to bounce off anisotropic surface along the opposite direction as the microstructure, and the bouncing distance and rebound angle would be greater due to t_0, n_1, and l_1 being increased with the rise of the impacting height. When $h_0 > h_c$, the one part of microstructure contacted with liquid droplet remains only wet the top of microstructure, while another part would wet the whole of micro-gap due to the dynamic pressure being greater than the Laplace pressure. And then the droplet bouncing motion is determined by the competition between I_1 and I_2 due to the liquid droplet contact with the microstructure being in a composite state. If the effect of I_1 is dominant, the droplet would still show a backward motion. Yet, n_1, and l_1 would be reduced for the contact mode changing with increasing of impacting height. Hence, the droplet gradually changes from a backward motion to a forward motion, which would present a vertical motion when I_1 and I_2 are in balance in microstructural direction. Figure 3f presents the phase graph of droplet bouncing motion transitions on the anisotropic surface with the space of 300–800 μm. For larger space, its critical Weber number is smaller, easily presenting a forward motion. Inferring from the Weber number ($We = 2\rho g h_0 r_0/\gamma$), its critical impacting height (h_0) is smaller for larger droplets (r_0). Thus, the larger droplet would easily present a forward motion.

2.4. Long-Range Transport of Forward and Backward Motion

Long-range transport of droplets on the solid surface being a significant challenge for functional devices with anisotropic microstructures. Therefore, investigating a convey way with low-energy and long-distance is significant in applications. To characterize the transport sustainability and energy consumption of

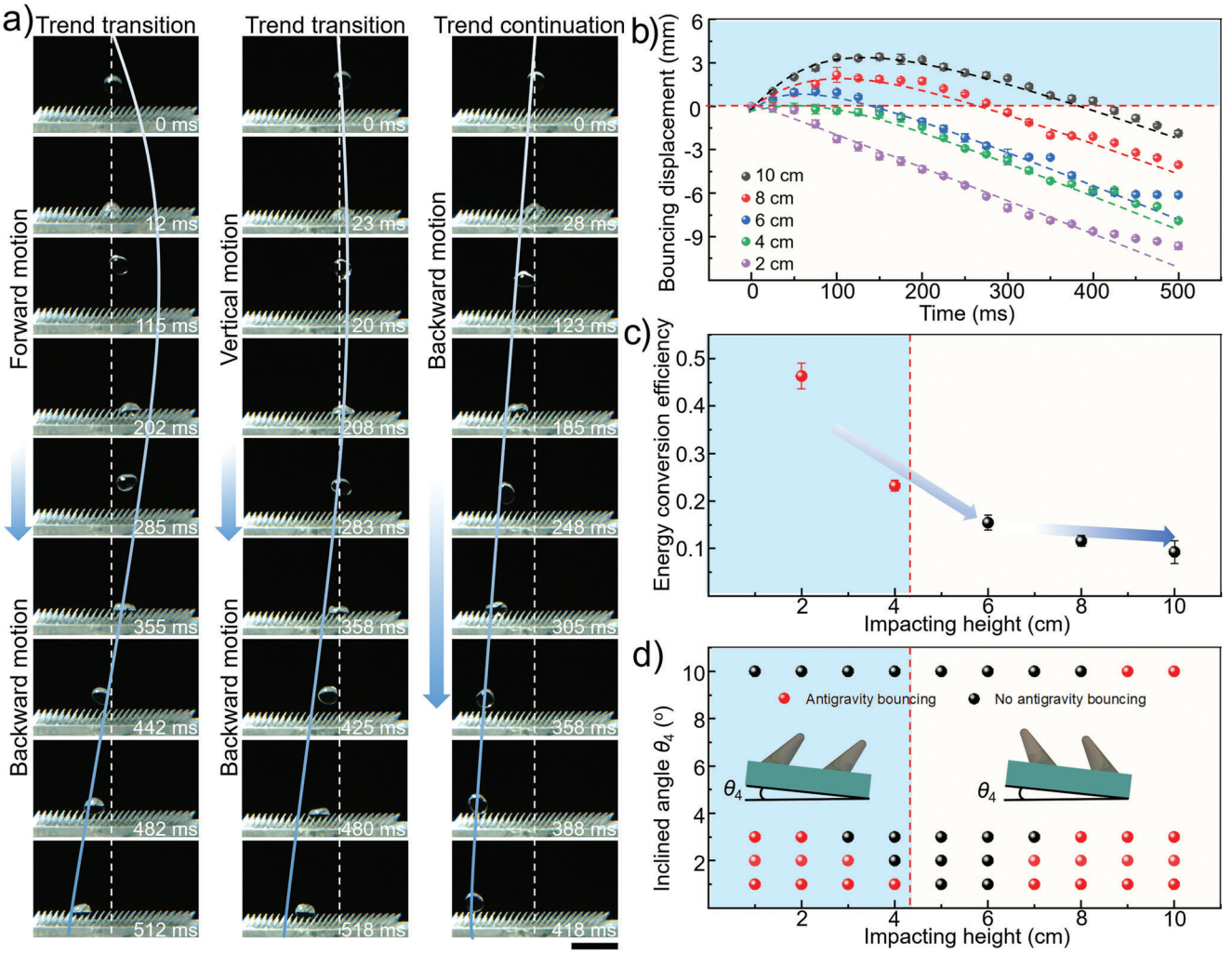

Figure 4. Long-range transport of forward and backward motion. a) The evolution of forward, vertical, and backward motions on the anisotropic surface. With dotted lines mark the centerline of liquid droplet, and scale bar is 2 mm (Movie S3, Supporting Information). b) Statistical results of transport displacement of liquid droplet with impacting heights of 2, 4, 6, 8, and 10 cm. c) Energy conversion efficiency of liquid droplet at diverse impacting heights. Detailed of energy conversion efficiency analyzed is presented in Experimental Section. d) Phase diagram anti-gravity motion of liquid droplet on the tilted surface. The tested surface with tilting angles is 1°, 2°, 3°, and 10°, respectively (Figure S4 and Movie S4, Supporting Information).

different bouncing motions, we investigate the evolution of liquid droplet motion at a range of impacting heights (**Figure 4**a). Observations present that regardless of whether the initial motion is forward or vertical, the droplet ultimately present a backward motion when the impacting velocity lower than the critical velocity. Therefore, even if the droplet with a large impacting velocity shows a forward motion, it bouncing direction would turn into the opposite direction, bouncing back to initial position. This type of bouncing motion would not be preferable in the long-range transport application. In comparison, the liquid droplet with a low impacting velocity shows a backward motion with a lager bouncing displacement at the end (Figure 4b). In addition, energy balance analysis reveals that the energy conversion efficiency of backward and forward motion is 46.3% and 9.3%, respectively. The disparity in energy conversion efficiency between these two types of bouncing motions can be as much as fivefold (Figure 4c). Considering the displacement and energy consumption, the backward motion would an attractive way for long-range transport of droplets. Ultimately, we also compare the performance of two types of bouncing motions in anti-gravity delivery. The phase diagram presented in Figure 4d illustrate that the backward motion at a lower stimulus speed enables an anti-gravity delivery while the forward motion requires a higher impacting speed to achieve the same. Yet, at a large tile angle of surface, the backward motion is unable to achieve anti-gravity motion.

3. Discussion

Above, we have provided experimental evidence of the velocity-switched droplet rebound direction on the anisotropic surface. Observations present that, as the impacting height increases from 2 to 10 cm, the liquid droplet successively shows a backward, vertical, and forward motion after impacting on the asymmetric surface. In contrast to previous studies, this study

provides the first experimental evidence that the rebound direction of a droplet impacted on the asymmetric surface is not only determined by surface properties but also affected by the initial impacting condition. Characterized by the liquid–solid interaction, it is revealed that the transition in the liquid rebound direction is accompanied by a contact state change. Analyzed from the perspective of force balance, it is demonstrated that the contact state of a liquid droplet on the anisotropic surface is determined by the competition of droplet dynamic pressure and the Laplace pressure in the microstructure, and the critical velocity is expressed as $v_c = \sqrt{16\gamma_{lv}\delta/(\rho l_1^2)}$. The droplet wet the top of microstructure and is loaded by a surface tension along the opposite microstructural direction when the dynamic pressure is less than the microstructural Laplace pressure, otherwise wet the whole of microstructure and is loaded by a surface tension along the microstructural direction. Therefore, even if the asymmetric surface has been fabricated, a broad range of bouncing motion can still be achieved by a designed initial velocity. This work, including experiments, theoretical models, and dynamics analysis provides valuable insight view into the droplet motions on the anisotropic surface and the functional surface designing.

The directed, long-range, and self-propelled transport of droplets on solid surfaces plays a crucial role in various applications, ranging from harvesting to bio-analysis. Typically, preferential transport is achieved by topographic or chemical modulation of surface wetting gradients that break the asymmetric contact line and overcome the resistance force to move droplets along a particular direction. In contrast to complex chemical modulation, the liquid transport on the asymmetric surface is a physical and straightforward approach. In this work, we detailed investigate the transport displacement and the energy conversion efficiency in long-range transport. The results reveal that, regardless of the initial motion is forward or vertical, the droplet ultimately present a backward motion due to the decrease in impacting velocity. And the droplet with a backward motion on the anisotropic surface remain its transport direction until it stops moving. In addition, the energy conversion efficiency indicates that the droplet with a backward motion can efficiently convert vertical kinetic energy into horizontal kinetic energy, which reaches 45.8%. Comparative analysis reveals that the energy conversion efficiency in backward motion is three times than that in forward motion, which may be attributed to the different contact states during the transport process (Corresponding to Figures 3 and 4). Therefore, the backward bouncing motion would be preferred in long-range transport due to the high energy conversion efficiency and sustainability.

4. Conclusion

Herein, we present that the liquid droplet rebound direction on the anisotropic surface can be switched by controlling the impacting velocity. Observations show that the liquid droplet successively shows a backward, vertical, and forward motion on the asymmetric surface increases from 2 to 10 cm. Characterized by the liquid–solid interaction and analyzed from the perspective of loading force, it is demonstrated that the contact state and resultant force induced by microstructures determines the bouncing motion on the anisotropic surface, which presents diverse performance at different impacting velocity. The critical velocity and impacting height are described by $\sqrt{16\gamma_{lv}\delta/(\rho l_1^2)}$ and $8\gamma_{lv}\delta/\rho g l_1^2$. Furthermore, the backward motion is preferred in long-range transport due to the high energy conversion efficiency and transport sustainability. With its advantages, this study highlights that the initial impacting condition is another principal factor to alter the droplet rebound direction. This finding is expected to garner significant interest from academia and industry, potentially promoting the practical applications of "backward transport".

5. Experimental Section

Preparation of Anisotropic Superhydrophobic Surfaces: The superhydrophobic tilted micro cone array was achieved by soft lithography and crystal growth methods (Figure S1a, Supporting Information). This structure was achieved through a 3D dispensing machine, and the entire process was fully automatic. A steel needle was equipped on the 3D dispensing machine and it was inserted into the PVC template at an oblique angle for producing the hole arrays. Polydimethylsiloxane (PDMS, Sylgard 184) and the curing solution were mixed with the weight ratio of 10:1 for duplicating the flexible tile cone arrays. The PDMS prepolymer was poured on the surface of the template, and after removing the excess gas inside by vacuuming, then it was placed on a heating plate at 80 °C for 2 h. After the PDMS wa cured, it was stripped from the template surface to obtain a structure with an anisotropic cone array. After being modified by ZnO nano-rod and (Heptadecafluoro-1,1,2,2-tetradecyl) trimethoxysilane (FAS-17), the surface was equipped with superhydrophobic function. Gallium, indium, and zinc were melted at a mass ratio of 89.5:10:0.5 at 150 °C to form alloy, which was used to generate crystal seed on the PDMS surface. The liquid metal was repeatedly rubbed on the surface of the sample until the surface of the sample was all black, and then the excess liquid metal was removed. After being cleaned with deionized water for > 1 min, the sample could be placed in a 100 mL reactor to prepare and grow the liquid for reaction. Hexamethylenetetramine (0.30 g) and 0.72 g of $Zn(NO_3)_2{\cdot}6H_2O$ were mixed into 100 mL of deionized water and reacted with the PDMS in a reactor at 85 °C for 12 h to generate ZnO nanorod. After the sample with ZnO nano-rod was washed by deionized water and dried, FAS-17 was used to tailor the surface energy of the as-fabricated samples at 90 °C for 5 h (at a vacuum degree of 0.1 MPa).

Electron Microscopy and Wettability Characterization of Anisotropic Superhydrophobic Surfaces: Observation of the topographies of anisotropic superhydrophobic surfaces and the characterization of ZnO nano-rods were obtained by environmental scanning electron microscopy (ESEM, Quanta FEG-250, FEI, USA) at a voltage of 10–15 kV. The contact angle of a liquid droplet with a volume of 10 µL on the anisotropic superhydrophobic surfaces was tested by a video-based contact angle measuring device (OCA 20, Dataphysics, Germany) with a precision of $\pm 0.1^{\circ}$.

Characterization of Droplet Bouncing Motion: The droplet was injected by a micro pump (Pump 11 Elite, Harvard Apparatus, USA) to impact the anisotropic superhydrophobic surfaces. Observation of the droplet bouncing motion was recorded by a high speed camera (CrashCam Stick HD, America) mounted on an independent *XYZ* stage at 1000 frames per second. The displacement of the droplet was obtained by using ImageJ software.

Supporting Information

Supporting Information is available from the Wiley Online Library or from the author.

Acknowledgements

This work was supported by the National Natural Science Foundation of China (no. 21805294).

Conflict of Interest

The authors declare no conflict of interest.

Author Contributions

P.L. and F.Z. contributed equally to this work. L.W. conceptualized the idea and supervised the research. P.L. and F.Z. conceived the idea, designed the experiment, collected the datasets, and drafted the manuscript. All authors read, contributed to the discussion, and approved the final manuscript.

Data Availability Statement

The data that support the findings of this study are available from the corresponding author upon reasonable request.

Keywords

anisotropic superhydrophobic surface, bouncing motion, droplet transport, energy conversion, impacting velocity

Received: July 4, 2023
Revised: August 14, 2023
Published online: September 26, 2023

[1] H. A. Stone, A. D. Stroock, A. Ajdari, *Annu. Rev. Fluid Mech.* **2004**, *36*, 381.
[2] M. Nosonovsky, B. Bhushan, *Curr. Opin. Colloid Interface Sci.* **2009**, *14*, 270.
[3] T. S. Wong, S. H. Kang, S. K. Y. Tang, E. J. Smythe, B. D. Hatton, A. Grinthal, J. Aizenberg, *Nature* **2011**, *477*, 443.
[4] T. M. Schutzius, S. Jung, T. Maitra, G. Graeber, M. Köhme, D. Poulikakos, *Nature* **2015**, *527*, 82.
[5] S. Feng, J. Delannoy, A. Malod, H. Zheng, D. Quéré, Z. Wang, *Sci. Adv.* **2020**, *6*, eabb4540.
[6] G. D. Bixler, B. Bhushan, *Nanoscale* **2013**, *5*, 7685.
[7] K. Liu, X. Yao, L. Jiang, *Chem. Soc. Rev.* **2010**, *39*, 3240.
[8] P. Li, B. Zhang, H. Zhao, L. Zhang, Z. Wang, X. Xu, T. Fu, X. Wang, Y. Hou, Y. Fan, L. Wang, *Langmuir* **2018**, *34*, 12482.
[9] J. Li, Y. Hou, Y. Liu, C. Hao, M. Li, M. K. Chaudhury, S. Yao, Z. Wang, *Nat. Phys.* **2016**, *12*, 606.
[10] P. Li, X. Xu, Y. Yu, L. Wang, B. Ji, *ACS Appl. Mater. Interfaces* **2021**, *13*, 27687.
[11] W. Xu, Y. Jin, W. Li, Y. Song, S. Gao, B. Zhang, L. Wang, M. Cui, X. Yan, Z. Wang, Z. K. Wang, *Sci. Adv.* **2022**, *8*, ade2085.
[12] J. T. Feng, F. C. Wang, Y.-P. Zhao, *Biomicrofluidics* **2009**, *3*, 022406.
[13] D. Tian, N. Zhang, X. Zheng, G. Hou, Y. Tian, Y. Du, L. Jiang, S. X. Dou, *ACS Nano* **2016**, *10*, 6220.
[14] A. Li, H. Li, Z. Li, Z. Zhao, K. Li, M. Li, Y. Song, *Sci. Adv.* **2020**, *6*, eaay5808.
[15] X. Xu, T. Qian, *Phys. Rev. E* **2012**, *85*, 051601.
[16] Q. Dai, W. Huang, X. Wang, M. M. Khonsari, *Langmuir* **2018**, *34*, 3806.
[17] S. Sakurada, M. Sole-Gras, K. Christensen, D. B. Wallace, Y. Huang, *Addit. Manuf.* **2020**, *31*, 100934.
[18] Y. Liu, L. Moevius, X. Xu, T. Qian, J. M. Yeomans, Z. Wang, *Nat. Phys.* **2014**, *10*, 515.
[19] D. Debnath, D. Verma, P. Kumar, V. Balakrishnan, *Int. J. Multiphas. Flow* **2023**, *159*, 104344.
[20] M. H. Biroun, M. Rahmati, R. Tao, H. Torun, M. Jangi, Y. Fu, *Langmuir* **2020**, *36*, 10175.
[21] C. Hao, Y. Liu, X. Chen, J. Li, M. Zhang, Y. Zhao, Z. Wang, *Small* **2016**, *12*, 1825.
[22] L. Jin, Y. Wang, *Colloid Interface Sci. Commun.* **2021**, *44*, 100495.
[23] K. Lippera, M. Benzaquen, S. Michelin, *Phys. Rev. Fluids* **2020**, *5*, 032201.
[24] V. Liimatainen, M. Vuckovac, V. Jokinen, V. Sariola, M. J. Hokkanen, Q. Zhou, R. H. A. Ras, *Nat. Commun.* **2017**, *8*,1798.
[25] H. Chen, P. Zhang, L. Zhang, H. Liu, Y. Jiang, D. Zhang, Z. Han, L. Jiang, *Nature* **2016**, *532*, 85.
[26] W. Fang, K. Zhang, Q. Jiang, C. Lv, C. Sun, Q. Li, Y. Song, X.-Q. Feng, *Appl. Phys. Lett.* **2022**, *121*, 210501.
[27] J. Wang, Z. Zhu, P. Liu, S. Yi, L. Peng, Z. Yang, X. Tian, L. Jiang, *Adv. Sci.* **2021**, *8*, 2103182.
[28] Y. Liu, G. Whyman, E. Bormashenko, C. Hao, Z. Wang, *Appl. Phys. Lett.* **2015**, *107*, 051604.
[29] S. Daniel, M. K. Chaudhury, J. C. Chen, *Science* **2001**, *291*, 633.
[30] K. Ichimura, S. K. Oh, M. Nakagawa, *Science* **2000**, *288*, 1624.
[31] Q. Sun, D. Wang, Y. Li, J. Zhang, S. Ye, J. Cui, L. Chen, Z. Wang, H. J. Butt, D. Vollmer, X. Deng, *Nat. Mater.* **2019**, *18*, 936.
[32] Q. Zheng, C. Lv, P. Hao, J. Sheridan, *Sci. China Phys. Mech. Astron.* **2010**, *53*, 2245.
[33] Z. Zhao, H. Li, A. Li, W. Fang, Z. Cai, M. Li, X. Feng, Y. Song, *Nat. Commun.* **2021**, *12*, 6899.
[34] H. Li, W. Fang, Y. Li, Q. Yang, M. Li, Q. Li, X.-Q. Feng, Y. Song, *Nat. Commun.* **2019**, *10*, 950.
[35] S. Z. Wang, X. Huang, L. Chen, Y. S. Yu, *Phys. Fluids* **2023**, *35*, 027118.
[36] M. Reyssat, A. Pépin, F. Marty, Y. Chen, D. Quéré, *Europhys. Lett.* **2006**, *74*, 306.
[37] H. Bai, X. Wang, Z. Li, H. Wen, Y. Yang, M. Li, M. Cao, *Adv. Mater.* **2023**, *35*, 2211596.
[38] Y. P. Zhao, *Physical Mechanics of Surfaces and Interfaces [M].*, Beijing: Science Press **2012**.
[39] Y. P. Zhao, *Nano and Mesoscopic Mechanics [M].*, Beijing: Science Press **2014**.
[40] Z. X. Cai, F. Z. Chen, Y. L. Tian, D. W. Zhang, Z. X. Lian, M. Y. Cao, *Chem. Eng. J.* **2022**, *449*, 137831.